

Laser Joining of Continuous Glass Fiber Composite Preforms

Huade Tan

Graduate Research Assistant
e-mail: ht2288@columbia.edu

Y. Lawrence Yao

Professor
Fellow ASME
e-mail: yly1@columbia.edu

Department of Mechanical Engineering,
Manufacturing Research Laboratory,
Columbia University,
NY 10027

A laser fusion joining method is investigated for the purpose of through thickness strengthening of glass fiber reinforced laminate composites. Laser fusion joining is evaluated as a potential process to replace mechanical reinforcements used in conventional laminate composite fabrication. A two step laser process is developed to form fusion bonds between fibers within a single bundle and between adjacent fiber bundles. Coupled heat transfer and viscous flow modeling is carried out to investigate the temperature and dynamics of the joining process under three experimentally observed conditions. Linear elastic finite element analysis is used to investigate the effect of joint morphology on stress concentrations and strength. Joint strength is found to be a function of the fiber contact angle and packing density at the joint interface. Tensile tests show that laser joined fiber bundle strength is on the same order of magnitude as the raw fiber bundles. The challenges to laser processing of three dimensional fiber reinforcements in laminate composite fabrication are discussed. [DOI: 10.1115/1.4023270]

1 Introduction

Laminate fabrication is a widely applied method for the construction of layered continuous fiber reinforced polymer matrix composites using either prematrix impregnated (prepreg) or non-impregnated fabrics. Laminate fabrication using prepreg materials involves the layering (lay-up) of densely packed layers (plies) of resin infused fiber reinforcement tape to produce thin shell structures with desired strength and stiffness properties in the layer directions [1]. Laminate composites manufactured from prepreg materials exhibit high fiber packing fractions and high strength along fiber directions, with no fiber reinforcements in the thickness direction due to the lay-up construction process. Prepreg material construction is undesirable for composites requiring high through thickness strength and fracture toughness. The insertion of mechanical reinforcements (z pins) through layers of prepreg fabrics has been shown to improve the through thickness strength of prepreg laminate composites [2,3]. Z pinning increases the through thickness strength by bridging inter laminar cracks, relying on matrix material properties and friction to transfer stresses and loads between the fibers and pins. The insertion of z pins has also been shown to displace in plane fibers and introduces pockets of resin rich regions near the pins. These resin rich regions act as stress concentrations in planar loading conditions, resulting in reduced planar strength.

Investigations into laminate fabrication methods for improved through thickness strength have led to the development of non-impregnated fiber fabrics in three dimensional structures (preforms) which are infused with the matrix using a resin infusion process such as vacuum assisted resin transfer molding. Such methods have been shown to produce composites with desirable fiber packing and significant improvements in the through thickness strength [4,5]. Through thickness strength is achieved by distributing reinforcement fibers in the z direction commonly referred to as 3D weaving [6,7]. In the case of 3D woven reinforcements, as is similar to z pinning, out of plane fibers are separated from in plane fibers by the matrix material. Thick 3D woven fabrics have also been shown to improve fiber placement accuracy and reduce labor costs by reducing the number of plies required in the laminate lay-up and vacuum infusion processes. A major pro-

cess complication of 3D woven preform fabrication, however, is the cost and complexity of the machinery required in the weaving process. The fiber architecture of a 3D woven preform is dictated by the mechanical looms required in the weaving process [4,8]. Laminates requiring nonconstant thicknesses or irregular geometries require secondary machining steps or discontinuous fabric placement during fabric lay-up, adding to the cost of the process and impairing the interlaminar strength of the material. While 3D weaving has been shown to yield significant improvements in through thickness strength within a single layer of thick reinforced fabric, laminate construction using multiple layers of 3D woven fabrics lacks fiber reinforcement between lamina, where the risk of delamination is greatest. The introduction of woven fibers or stitching in the thickness direction also displaces fibers in the planar directions and introduces resin rich regions, similar to z-pinning techniques. A comparable process to 3D weaving with a lower equipment cost and greater manufacturing flexibility is desirable.

The use of near infrared lasers to join thermoplastic fabrics [9,10] presents an alternative process to 3D weaving, offering similar mechanical enhancements at reduced manufacturing complexity and equipment costs. Textile applications that require high strength, high precision, seamless joints such as air bags, medical fabrics and protective garments are candidates for such a laser process. In these applications, the added costs of laser processing are justified by high weld rates, localized joining, watertight sealing, and reduced labor costs. Laser joining of fibrous materials employs a direct fusion process unlike traditional mechanical or chemical bonding methods. Laser joining processes have been shown to offer better seam quality and strength compared to stitching or weaving processes. The development of laser fiber joining presents a direct application to 3D fiber preform fabrication.

Laser fusion joining presents possible advantages in strength over stitching, weaving or adhesion methods due to higher reinforcement density and direct fiber to fiber joining in both the axial and radial directions. Laser processing allows joints to be restricted to highly localized regions, i.e., regions of existing stress concentrations. Laser fiber joining requires less complicated equipment and allows for greater manufacturing flexibility in part geometry and fiber architecture than 3D weaving processes. Computer controlled fabric manipulation and processing using laser irradiation to concurrently cut and join textiles reduces material waste through precise fiber usage and placement. High weld rates may be achieved with existing laser and optics technologies.

Contributed by the Manufacturing Engineering Division of ASME for publication in the JOURNAL OF MANUFACTURING SCIENCE AND ENGINEERING. Manuscript received April 12, 2012; final manuscript received December 26, 2012; published online January 22, 2013. Assoc. Editor: Wei Li.

A physical challenge in the fusion joining of woven fibers, as observed in textile joining investigations [9,10], is the tendency of the melt pool to flow away from the desired joint region, forming voids in the processing zone. Both woven textiles and composite preforms are composed of many bundles of fibers, each of which is composed of hundreds of individual fibers. Due to fiber fusion and compaction processes observed during joining [11,12], the total volume fraction of glass in a fused joint is much greater than in the initial fiber bundle. When fibers are heated to the glass transition temperature, the fiber structure rapidly compacts and increases in density, as observed in studies of the sintering of particulates due to viscous flow [13]. During this process the density of the fiber structure relative to bulk glass rapidly increases as fibers fuse together to form a joint. When fibers are heated locally with a laser, a large density gradient develops between the joint and the fiber bundle. Capillarity effects drive the melt pool to flow in the direction of the density gradient, resulting in the undesirable formation of voids at the laser spot. Densification induced void formation leads to low material connectivity and strength across the joint. In order to achieve fusion joining of 3D fiber preforms, we investigate the technical challenges inherent in the fiber fusion process.

One solution to both the densification and void formation problem has been to introduce a filler material into the joint. Filler materials of desirable absorption properties at 1064 nm wavelength, developed for transparent lap joining of thermoplastic materials, have been used successfully in the laser lap joining of thermoplastic fabrics [9]. Such fillers are composed of proprietary polymers, adding cost and complexity to the joining process. No such filler materials have been developed for glass. A similar solution to overcoming the fiber spacing and flow problems is required to accomplish fiber fusion joining of glass reinforcements.

A two step laser joining process for glass fiber reinforcement preforms is developed to overcome the void formation problem. This process compensates for the compaction and flow behavior of the fiber bundle during fusion and uses the existing fiber material to achieve dense joints. Numerical solutions using a two-phase temperature-dependent viscous flow model are shown to reproduce the melt flow pattern and joint morphology during a fusion joining process. Coupled temperature-dependent viscous flow modeling is used to characterize the effects of surface tension and viscosity on joint morphology and dynamics during processing. Finite element analysis is performed to determine the effect of joint morphology on local stress concentration factors. Lessons learned from the effects of the fiber contact angle and packing density on joint strength as observed in single bundle tensile tests yield insights into producing through thickness reinforced 3D joined preforms.

2 Experimental Setup

Laser joining of E-glass fibers was achieved using a 2 kW Nd:YAg laser (GSI Luminotics) operating at a range of 30 W–120 W. All glass samples consist of 99.98% E-glass plain weave fabric. Samples were prepared from six ounce per yard plain woven fabric with 18 bundles of fiber per inch and 300 fibers per bundle. The Gaussian laser spot was defocused to a diameter of 2 mm to allow for more uniform irradiation of a single fiber bundle. Motion control was accomplished using a Staubli six axis robotic manipulator with a flat, square grid sample holder to facilitate fiber placement.

Tensile testing of single bundle and seam welded plain weave samples were performed on an Instron material testing system with a 2 kN load cell at a rate of 0.5 millimeters per second. Single bundle fiber tension tests were performed using grooved cylindrical grips available from Instron, allowing for uniform fiber gripping and confinement. Each sample was composed of two nine inch long fiber bundles joined in the center. Fiber bundle samples were wound around grooves in each grip such that the joint was centered between the grips when loaded in tension. Joint

and fiber fracture surfaces were imaged using scanning electron microscopy (SEM) post mortem to evaluate the failure mechanisms due to tensile testing. Fracture surface images are compared to the stress concentrations results obtained from mechanical finite element modeling and observations during tensile testing to determine sources of stress concentrations and the cause of joint failure.

E-glass is highly transmitting at the 1064 nm wavelength. It was observed that densely packed E-glass fibers are of sufficient opacity to initiate heat accumulation. Infrared absorption within highly transmitting materials due to multiple surface scattering has previously been observed in investigations of densely packed beds of glass spheres [14] and porous media [15]. Absorption of glass is also known to be highly dependent on temperature [16,17]. Glass simultaneously absorbs and emits a wide range of wavelengths near the phase transition temperature [18,19].

Although other laser textile applications have evaluated the use of absorptive coatings for heat accumulation, it was determined from initial irradiation trials that surface coatings induce uneven absorption and poor joint density. Chemical reactions and oxidation occurs in fibers with surface sizing agents owing to the localized heating and a dramatic increase in laser absorption at elevated temperatures [16,19]. Temperature becomes uncontrollable once vaporization initiates. If the melt pool is allowed to exceed the vaporization temperature, ionization occurs very quickly, and the resulting plasma generated consumes the melt pool and any surrounding fiber material within a few spot radii. Uniform thermal absorption throughout the target spot is desired.

The dominant material transport process for glass fusion and densification processes is viscous flow due to surface tension, as cited in glass sintering processes [13,20]. As the melt volume increases, gravitational force becomes significant compared to the capillary and surface tension, leading to sagging of the melt pool. A particular challenge to fusion joining of fibrous systems is the high surface area and low relative density of the initial fiber structure. The joining method devised in this work derives from the need to compensate for the viscous flow effects inherent in the fiber material system. Numerical modeling of the glass fusion and densification during laser processing is undertaken to better understand the behavior of densely packed glass fibers under experimentally observed conditions.

3 Numerical Simulation

3.1 Two-Phase Thermal Viscous Flow Model. A two dimensional two-phase fluid heat transfer compressible flow model is implemented to simulate the flow behavior of the molten pool during fiber joining. The simulation concurrently solves the compressible Navier–Stokes equations for viscous fluid flow, phase field (Cahn–Hilliard) equations [21,22] for two-phase immiscibility and velocity dependent heat equations. Phase, density, and temperature evolution output from the multiphysics model yield spatially resolved time dependent flow of glass during laser processing.

Laminar viscous flow is captured by solving the compressible Navier–Stokes equations

$$\rho \frac{\partial \mathbf{u}}{\partial t} + \rho(\mathbf{u} \cdot \nabla) \mathbf{u} = \nabla \cdot \left[-p \mathbf{I} + \eta (\nabla \mathbf{u} + (\nabla \mathbf{u})^T) - \frac{2}{3} \eta (\nabla \cdot \mathbf{u}) \mathbf{I} \right] + \mathbf{F},$$

$$\frac{\partial \rho}{\partial t} + \nabla \cdot (\rho \mathbf{u}) = 0 \quad (1)$$

where ρ and η are the density and dynamic viscosity of E-glass, and \mathbf{u} is the velocity field of the melt pool. During laser processing simulations, glass and air are solved in separate fluid domains. Phase field equations are used to track the domain interfaces between air and glass such that at the interface, a continuous phase variable ϕ is defined by Refs. [21,22]

$$\frac{\partial \phi}{\partial t} + \mathbf{u} \cdot \nabla \phi = \nabla \cdot \frac{3\chi\epsilon\sigma}{2\sqrt{2}} \nabla \Psi \quad (2)$$

$$\Psi = -\nabla \cdot \epsilon^2 \nabla \phi + (\phi^2 - 1)\phi + \frac{\epsilon 2\sqrt{2}}{3\sigma} \frac{\partial f}{\partial \phi} \quad (3)$$

where ϕ is the continuous phase variable in the limits of ± 1 , $D = 3\chi\epsilon\sigma/2\sqrt{2}$ is the diffusion coefficient of the phase boundary defined by the interface mobility parameter $\chi = \begin{cases} 0 & T < T_i \\ 1 & T \geq T_i \end{cases}$, where $T = 1200$ K, surface tension coefficient σ , and the phase transition region ϵ given by as half the maximum element size $\frac{1}{2}h_{\max}$. Throughout the simulation, heat transfer within and between the two fluids is solved through the velocity dependent heat equation

$$\rho C_p \frac{\partial T}{\partial t} + \rho C_p \mathbf{u} \cdot \nabla T = \nabla \cdot (k \nabla T) + Q \quad (4)$$

where, C_p , k are the density, heat capacity and thermal conductivity of each fluid phase, and Q is a spatially resolved laser energy input given by

$$Q(x, y) \left[\frac{W}{m^2} \right] = \alpha Q_M e^{-\frac{(x-x_0)^2}{2d_x^2} - \frac{(y-y_0)^2}{2d_y^2}} V_{F_{\text{glass}}} \quad (5)$$

Given a symmetric spot diameter of 2 mm, the laser energy input into the system fits a Gaussian distribution defined by $d_x = d_y = 0.25$ mm. The peak power density Q_M of the laser is assumed to be the reciprocal of the area integral of the Gaussian, which is approximately three times ($\int_0^{2\pi} \int_0^\infty e^{-8r^2} dr d\theta^{-1} = 8/\pi$) the continuous beam power, such that the total energy input into the model matches the laser energy output. A constant absorption fraction $\alpha = 0.3$ is used to adjust the simulation output to match the temperature profile of the melt pool to that of molten glass during joining. The laser energy is applied only in the glass phase ($V_{F_{\text{glass}}}$) which corresponds to the phase condition $\phi > 0$ from the Cahn–Hilliard equations.

As glass undergoes a phase transition, the flow rate of the glass phase is highly coupled to the temperature-dependent viscosity by the Vogel–Fulcher–Tammann equation: given for E-glass as [23]

$$\eta(T) = 10^{-4.88 + \frac{6277}{T-268}} \quad (6)$$

where η is the dynamic viscosity [Pa · s] used in Eq. (1) and T is the temperature output from Eq. (4) in degrees celsius. It is due to this highly temperature-dependent viscosity that glass behaves both as a solid and a fluid during the simulation. It is observed that the localized temperatures achieved through laser heating coupled with the highly temperature-dependent viscosity dictates much of the physical response of the material during joining.

Fiber bundles undergo significant densification during the sintering process. As individual fibers melt and agglomerate, the partly dense fiber structure compacts to form a fully dense glass melt. The sintering dynamics and compaction process is not directly simulated. The glass fluid phase is instead assumed to undergo a density transition near the melt temperature and the melt is assumed to be fully dense once the transition temperature has been reached. A temperature-dependent phase density of glass, used in Eq. (1), is given as

$$\rho(T) = \rho_0 + \Delta\rho \left(\frac{1}{1 - e^{T-T_\Delta}} \right) \quad (7)$$

where ρ_0 is assumed to be the initial partial density of the fiber compact and $\rho_0 + \Delta\rho$ is taken to be the density of glass. The assumption of instantaneous fiber compaction is good if fiber

Table 1 Material properties used in numerical simulations

Parameter	Units	Value (glass)	Value (air)
P	kg/m ³	2540	1
C_p	kJ/kg K	0.84	1
H	Pa s	Eq. (6)	$\ll \eta_{\text{glass}}$
K	W/m K	Eq. (8)	0.03
σ	N/m	0.31	—
N	—	1.3	—

sintering dynamics occur significantly faster than the heat and viscous flow dynamics. For the laser processing of compact fiber bundles, the high surface area of the fiber bundles and high temperatures achieved dictate a very fast fiber to agglomeration process. High sintering rates are observed at such conditions in many sintering studies [12,13] and from experimental trials conducted.

At high temperatures, the diathermanous properties of glass have been shown to induce higher than expected heat transfer in furnaces and large melt pools than is possible through thermal conduction and convection effects alone. At sufficient temperatures, glass spontaneously emits and absorbs infrared radiation, leading to a temperature-dependent radiation factor in the thermal conductivity of glass given by

$$k = k_c + k_{\text{rad}} \\ k_{\text{rad}}(T) = \frac{16n^2\delta T^3}{3\gamma} \quad (8)$$

Here $k_c = 1.05$ is the bulk thermal conductivity of glass [W/m K], n is the refractive index of glass, δ is the Stefan–Boltzmann constant, and $\gamma = 1E - 3\text{m}$ is a geometric parameter relating to the absorption over the mean free path of the material [24,25]. The laminar fluid conduction heat transfer model uses this two part thermal conductivity parameter to capture glass temperature during laser processing in the glass transition range.

The tendency of the glass melt to flow into the fiber bundle is controlled by the densification and compaction of fibers at the melt boundary. Sintering strains at the melt interface due to surface tension and capillarity develop due to the structure of the densely packed fibers and the steep density gradient between the fiber bundle and the melt pool. A density gradient dependent body force is assumed to act on the melt volume given by

$$\mathbf{F} = \beta \nabla \rho V_{F_{\text{glass}}} \quad (9)$$

where \mathbf{F} is the densification force applied to the compressible Navier–Stokes Eq. (1) and β is a constant tuning parameter used

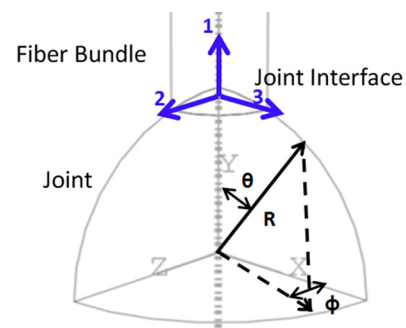


Fig. 1 Finite element model schematic of the outlining the Cartesian, material, and spherical coordinate axes defined with respect to an ideal spherical joint interface. For computational simplicity, one eighth of the joint geometry is modeled with symmetric boundary conditions on each of the dividing planes.

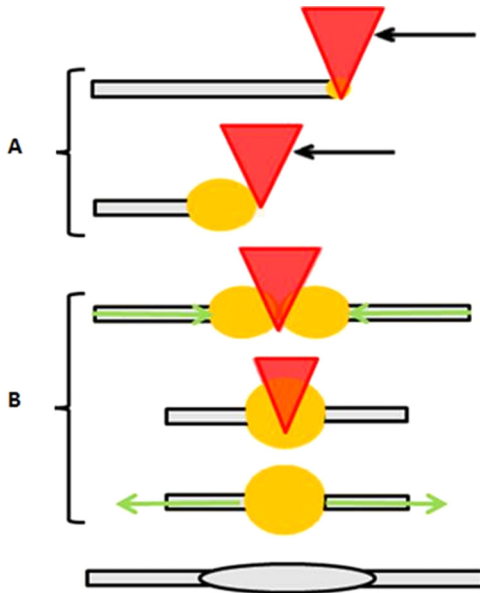


Fig. 2 (a) The laser fusion joining process schematic is presented showing the profile of a laser source scanning along a fiber bundle to initiate and propagate the melt bead formation process within a single bundle. (b) Joining is achieved between two preformed melt beads by irradiating both beads at the contacting point between the two bundles. A spherical bead is achievable if no mechanical constraints are applied on the melt pool during the joining process. Mechanical constraints or tension applied on the melt during the joining processes was found to result in ellipsoidal bead morphologies and tended to compact fibers in radial direction.

to match the morphology of the melt region during bead formation and joining processes. A value of $\beta = 0.1$ [Nm²/kg] was found to be adequate in simulations, but a more in depth derivation of the melt interface capillary force is lacking.

The set of coupled fluid, phase field, and thermal partial differential equations are solved concurrently using a spatially resolved finite element domain in a fully coupled backward Euler time integration scheme using COMSOL Multiphysics. The whole solution domain is discretized with a uniform 2D triangular mesh in order

to resolve the air/glass phase boundary throughout the simulation. Initial and boundary conditions specific for each processing condition as defined in Secs. 4.1–4.3. A list of the material properties used in this model is given in Table 1.

3.2 Mechanical Model. A linear elastic, static finite element analysis ($\sigma = E : \epsilon$) of a spherical body connected to a cylindrical bundle is used to simulate the stress state in a fiber joint (Fig. 1). Finite element simulations of idealized joint geometries under uniaxial tensile strain are performed in ABAQUS to determine the stress concentration factor in the fiber bundle near the bead joint. The spherical bead joint is assumed to be composed of a solid isotropic linear elastic material with the modulus and strength of soda lime glass. The cylindrical fiber bundle is defined to be a linear elastic orthotropic material consistent of glass fiber reinforced composite aligned to the y axis in Fig. 1 defined by engineering constants $E, G_{12}, G_{13}, G_{23}$, and ν_{ij} , where $\nu_{ij}/E_i = \nu_{ji}/E_j$. For computational simplicity, one eighth of the joint geometry is modeled. Symmetric boundary conditions are applied to the bisecting (x-y, y-z) planes. A fixed z displacement boundary condition is applied on the x-y plane bisecting the spherical bead.

The length of the entire model is defined to be 10 times a constant bundle diameter and the diameter of the sphere is varied to obtain different contact angles. The contact angle is defined as the maximum angle θ_{\max} from the y axis at which the cylinder intersects the sphere. A zero contact angle ($\theta_{\max} = 0$ deg) thus corresponds to a spherical joint of infinite radius and a 90 deg contact angle ($\theta_{\max} = 90$ deg) corresponds to a joint of the same radius as the bundle. Both the spherical and cylindrical domains are discretized using 3D swept tetrahedral elements refined at the joint/bundle interface.

Nodes on the x-z plane are fixed in the y direction only. A uniform finite displacement of 0.02% of the bundle diameter is applied to the nodes at the opposite end of the cylinder. A total strain ($\Delta L/L$) of 2×10^{-5} is applied on the cylindrical bundle at the z boundary. The spatially resolved stress state at the interface of the cylindrical bundle and spherical bead is obtained from each finite element simulation for distinct contact angles. From these numerical results, the stress concentration factor K is obtained to be

$$K = \frac{S_{\max}}{S_0} \quad (10)$$

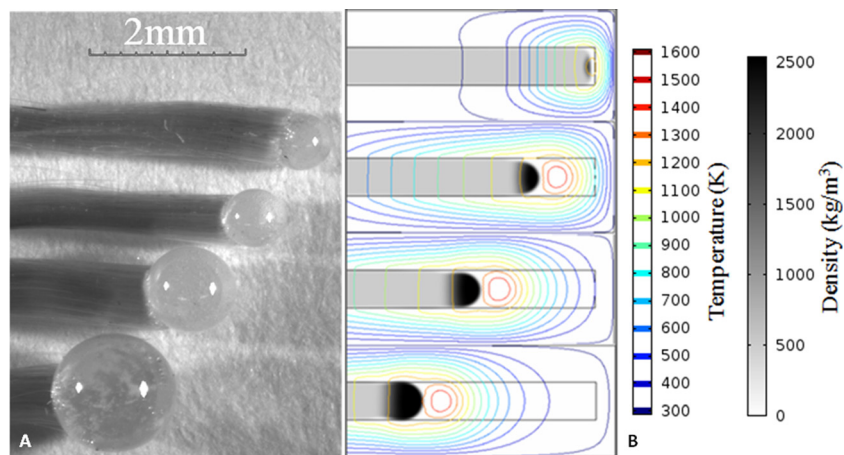


Fig. 3 (a) An optical micrograph of melt pools achieved by scanning the laser along the fiber bundle from one free end. On all samples the laser is scanned from right to left. Melt beads are arranged in increasing order of scan length from top to bottom. (b) Simulation output of the bead formation process depicted in order of increasing scanning length. Simulation snapshots are taken at 0.5, 3, 6 and 9 s from top to bottom.

where S_{\max} is the maximum principle stress component at the joint perimeter and S_0 is the uniaxial stress state of a uniform fiber bundle at the same strain. This ideal model assumes that both the fiber bundle and joint behave as fully dense continuum materials, capturing only the effect of the material isotropy mismatch during tensile testing on the stress concentration. The effects of fiber to fiber contact and bending stresses at the joint interface are not accounted for.

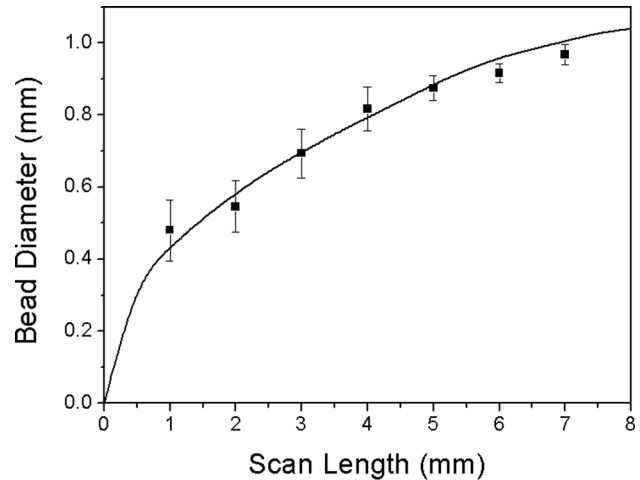
4 Results and Discussion

Laser processing challenges due to fiber bundle densification and void formation, as discussed in Sec. 1, are investigated in detail both experimentally and numerically in order to better understand the mechanics of the fiber fusion process. Fiber densification is investigated through the controlled formation and morphology characterization of the melt pool during laser processing at the free end of a single fiber bundle. The tendency of glass fibers to agglomerate and for the melt pool to minimize its surface energy is captured and discussed in the investigation of this bead formation process in Sec. 4.1. Void formation is investigated through the measurement of the melt separation during laser processing at the center of a fixed fiber bundle. Melt and void formation dynamics are captured and discussed in the melt separation process in Sec. 4.2. The laser fusion joining of two fiber bundles is carried out through the experimental trials and simulation of a two step fiber joining process as discussed in Sec. 4.3. The bundle joining process consists of a two step process, depicted in Fig. 2, developed from the lessons learned of the densification and void formation behaviors in Secs. 4.1 and 4.2.

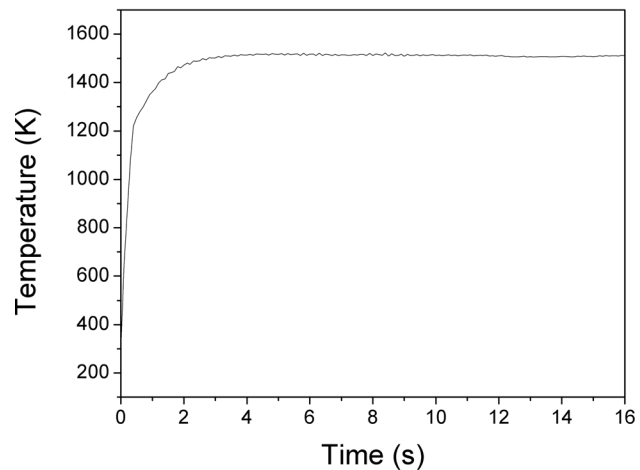
Mechanical testing and investigation of the fracture surfaces of the joints presented in Sec. 4.3 are conducted and discussed in Sec. 4.4. Fracture strength and behavior of fiber bundle joints are investigated as a function of the joint diameter and fiber packing fraction through tensile test data and joint morphology measurements. Fracture surfaces observed experimentally are compared to the stress concentration of the joint obtained through numerical simulation, confirming that there is a mechanical mechanism which limits the maximum strength achievable in this joining method.

4.1 Bead Formation. Fiber densification and flow during laser processing is investigated through the controlled experimental observation and simulation of the bead formation process at the free end of a single fiber bundle. Melt initiation and formation behaviors are studied in detail for E-glass fiber bundles exposed to a continuous 100 W laser source scanning at a rate of 0.5 mm/s along the fiber bundle axis, depicted in Fig. 2(a). At the transition temperature, glass is highly emissive and behaves as a viscous liquid. During laser processing, the melt bead is observed to emit visible light, from faint yellow and orange to white. Laser energy input into the fiber bundle is converted to heat and increases the temperature of glass to the point where the surface energy of the fibers is sufficient to overcome the resistance to viscous flow and induce densification [11,13]. During laser processing, fiber fusion and melt formation is observed to initiate at the center of the focal area, where the laser intensity is highest, and propagates rapidly outward.

Rapid fiber fusion and melt formation occurs at the laser spot between nearest fiber neighbors within the bundle, with fibers quickly shortening and agglomerating to lower their surface energy [26]. A melt pool is initiated at the center of the focus while nearby fibers are pulled into the melt pool. The melt pool rapidly collects into a spherical bead which tends to flow away from the laser spot. In order to continually heat the melt as the bead flows along the fiber bundle, the laser spot must follow the motion of the bead during laser processing. As the beam or the sample is translated at a constant velocity (0.5 mm/s) along the bundle axis the glass melt flows along the bundle in a stable quasi-static manner. As the melt bead flows ahead of the heat



(a)



(b)

Fig. 4 (a) Measurement results of the melt bead diameter obtained from microscopy images post processing versus scan distance plotted as markers with error bars signifying one standard deviation. Numerical results of the bead diameter versus scan distance are plotted in a solid line. (b) Temperature output plotted as a function of time. Note, given a scan speed of 0.5 mm/s, the scanning length of 8 mm corresponds to the 16 s. At this stable scanning speed, relative motion between the bead and the laser spot is zero.

source it increases in size by consuming additional fiber material. Bead morphology and sizes achieved through this laser scanning process are measured using optical microscopy as depicted in Fig. 3(a). Melt beads in Fig. 3(a) are presented in ascending order with respect to scan length and size. The monotonic relationship between scan length and diameter during bead formation processing is presented in the experimental results compiled in Fig. 4(a). From Fig. 4(a), a nonlinear monotonically increasing relationship between laser scan distance and bead diameter is observed. Given the initial 1 mm diameter of the fiber bundle, the melt pool does not collect into a regular spherical bead below a scan length of 1 mm and thus is difficult to measure experimentally. The scatter of the bead diameter data presented in Fig. 4(a) is observed to decrease with increasing scan length, due to reduced effects of fiber bundle and initial melt nonuniformity.

In order to better understand and characterize the fiber melt and densification mechanisms during laser processing, the bead formation process is simulated numerically. Coupled thermal and fluid modeling of the bead formation process is carried out with the

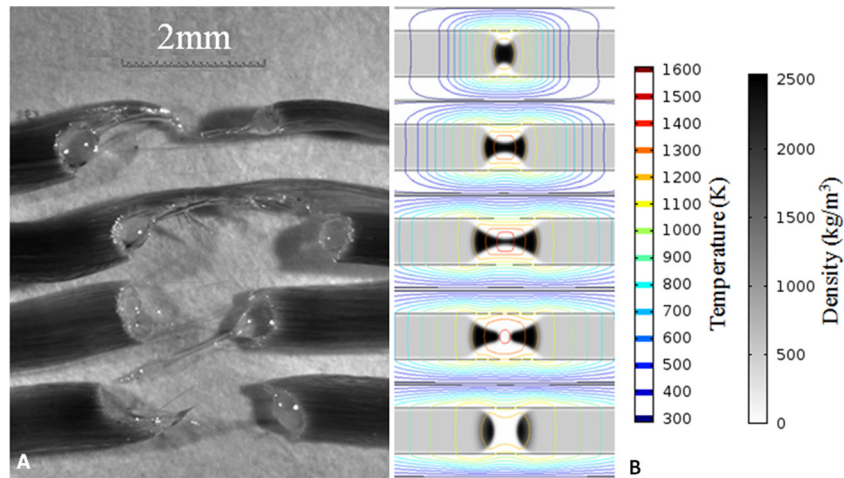


Fig. 5 (a) An optical micrograph of the melt morphologies of single bundle specimens irradiated at the center of the bundle while the ends were mechanically constrained. Melt samples are arranged in increasing order of laser exposure time from top to bottom. (b) Flow simulation output of the bundle separation process arranged in order of simulation time: 0.05, 0.20, 0.40, 0.45, and 2.0 s from top to bottom.

simulation of a Gaussian heat source moving along the center line of a continuous 2D rectangular bundle. The laser source is prescribed to start at time zero one spot radius away from the free end of the bundle. The fixed end of the bundle is prescribed to have a 90 deg contact angle with the boundary of the simulation domain. The domain boundary is prescribed to remain at room temperature throughout the simulation and allowed to have non-zero velocities throughout except at the surface where the bundle is attached. The phase, density, and temperature of the bundle and the environment are solved concurrently and the results obtained in a spatially resolved field within the simulation domain as a function of time. The temperature and density distribution of the fiber bundle are captured in snap shots of the simulation domain depicted in Fig. 3(b). Numerical results presented in Fig. 3(b) are arranged in ascending order with respect to simulation time and compares well with the experimental results in Fig. 3(a). The effects of bundle densification and flow dynamics on the morphology of the melt bead during laser processing are plotted as a function of scan length in Fig. 4(a). Simulation results of the bead diameter are shown to be monotonically increasing and in good agreement with the experimental findings plotted in the same figure.

The maximum temperature of the melt pool is plotted as a function of time in Fig. 4(b). Comparing the trend of the melt temperature and diameter obtained numerically in Figs. 4(a) and 4(b), it is observed that the glass material rapidly accumulates heat during the initial bead formation process prior to the steady flow behavior observed experimentally. After melt formation, the temperature of the bead plateaus and reaches a steady state as the flow of the bead matches the motion of the heat source. The control and manipulation of the melt morphology achieved during the laser scanning process investigated in this section will be compared to the undesired void formation behavior observed normally in laser fabric joining processes in Sec. 4.2 and extended to form controllable fiber bundle joints in Sec. 4.3.

4.2 Melt Separation. Laser processing induced void formation is studied by reproducing the behavior when exposing the center of a mechanically constrained fiber bundle with a stationary laser spot defocused to 2 mm diameter. The laser is operated at 30 W CW and the shutter exposure time is controlled to vary the total energy input into the target fiber bundle. The behavior of the melt pool in this configuration is dramatically different than what

was observed in Sec. 4.1. Laser processing at the center of a fiber bundle generates a melt pool connected to a fiber bundle at opposite ends causing the melt to be pulled in both directions by the capillary and densification forces acting along the fiber axis. Densification and flow effects act to thin and drive the melt pool away from the laser source in two directions. The bundle reduces in diameter continuously as the laser remains stationary. The melt is eventually pulled apart, forming two melt beads on either side of the laser spot, as depicted in Fig. 5(a). From Fig. 5(a), it is observed that the total glass volume of the bundle is conserved during processing and a poor joint is formed due to the reduction in cross-sectional area of the glass bundle.

After laser processing, the morphology of the melt pool is imaged and characterized using optical microscopy. The separation distance between the melt beads is measured from optical micrographs and plotted as a function of the laser exposure time in Fig. 6(a). From Fig. 6(a) it is observed that the fiber bundle separates rapidly and the distance between them ceases to expand near the diameter of the laser spot. Because the laser remains stationary throughout the process, the final separation distance is determined by the laser spot size, where the melt pool reaches the same quasi-static state observed in the bead formation process reviewed in Sec. 4.1. Increased laser exposure causes no further changes to the melt morphology.

The melt separation process is further investigated through the simulation of a 2D rectangular fluid domain with a stationary Gaussian heat input prescribed in the center. A rectangular fiber bundle is defined which bisects the computation domain and is constrained at two fixed boundaries, leaving no free ends. The simulation is carried out in the same manner as described in Sec. 4.1. Snap shots of the solution domain obtained from this model are presented in Fig. 5(b) in order of ascending exposure time. The simulation derived separation distance is plotted as a function of time in Fig. 6(a) along with experimental results. A sharp jump in the separation distance is observed in the simulation at time $t = 0.4$ s at the unstable separation point of the melt pool. The corresponding temperature history of the separation simulation is plotted in Fig. 6(b). The melt temperature is observed increase rapidly at time $t = 0$, when the fiber bundle is fully exposed to the laser source. As the melt diameter diminishes, so does the heat input into the fiber bundle such that the melt temperature begins to level off. At the unstable separation point, the molten glass pulls away from the center of the focus and the temperature of the melt pool drops rapidly. After the melt pool

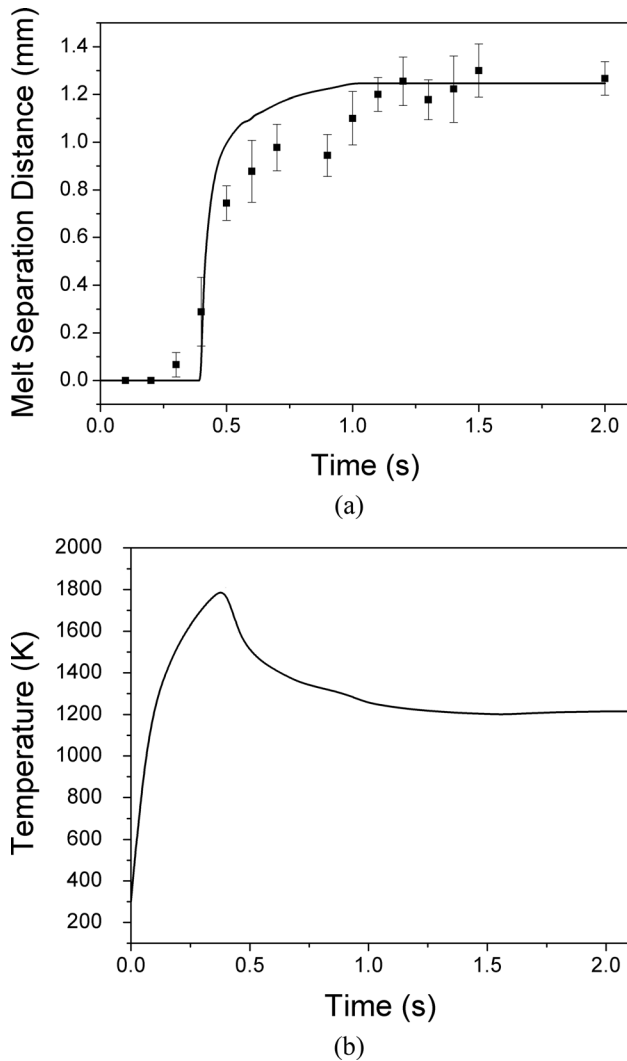


Fig. 6 (a) Melt separation distance measured from optical microscopy is plotted against laser exposure time as markers with error bars signifying one standard deviation. Simulation results of the separation distance between melt pools are plotted as a function of processing time in a solid line. (b) The maximum simulation melt temperature is plotted as a function of processing time. A very sudden separation behavior of the melt is captured in this model at time $t = 0.4$ s, as is characteristic of the void formation process observed during joining experiments. A stable melt temperature and separation distance is observed after the initial melt formation and separation instability.

separates, a constant temperature is observed in the two melt pools while the heat source is still on. This equilibrium temperature is below that observed in Fig. 4(b), the temperature required to maintain a steady flow in the melt, and thus the melt pools remain stationary and a maximum separation distance is achieved.

From the study of the melt separation and bead formation, it is apparent that the manipulation of laser power, focus and sample structure is required to control the temperature, densification and flow behavior of the glass fibers and glass melt. The knowledge of the densification process is extended to develop a laser joining process for two initially separate fiber bundles.

4.3 Bundle Joining. By extending the bead formation process presented in Sec. 4.1, a two part joining process is developed which mitigates the effects of melt separation observed in Sec. 4.2. In order to introduce excess glass material into the melt

pool, melt beads are first formed on two opposing fiber bundles prior to joining. Fused beads were found to readily absorb near infrared laser irradiation in later processes. After bead formation, two fiber bundles are brought into contact and irradiated to form a continuous joint, as depicted in Fig. 2(b). The total volume of the joint is determined by the initial volume of both beads and any additional fiber material accumulated during the joining process. Joint morphologies obtained from repeated bundle joining trials are depicted in Fig. 7. From Fig. 7, it is observed that the characteristic morphology of a joint formed between two melt beads on opposing fiber bundles is an ellipsoid. The ellipsoidal joint morphology derives from the competing surface tension forces investigated previously. Surface tension pulling the melt pool together to form a spherical bead is opposed by the tension at the fiber bundles pulling the melt pool apart. This fluid equilibrium yields a relatively stable process with a wide processing window compared to the unstable melt separation behavior observed in Sec. 4.2.

During joining experiments it was observed that applying tension on joined fiber bundles while cooling results in dramatic joint elongation. Spherical, elliptical and cylindrical or conically tapered morphologies are achievable by stretching the joint to various lengths during cooling, as depicted in Fig. 8. By stretching the joint during cooling, fiber packing density at the joint interface is also increased. The increase in fiber packing due to stretching is observed through SEM images of the fracture surface of both joint types in Fig. 9. The effects of stretching and fiber packing density on joint strength and fracture behavior will be discussed further in Sec. 4.4.

To better understand the dynamics of the joining method, the process is modeled by two opposing bundles connected to two circular beads meeting at the center of the solution domain. A stationary Gaussian 30 W laser thermal input is centered at the contact point of the two beads. Fluid flow and heat transfer equations are solved concurrently in the same manner as discussed in Secs. 4.1 and 4.2. Snap shots of the joint morphology and temperature distribution in the solution domain are presented in Fig. 7 in ascending order of the solution time. Qualitative comparisons between experimental and numerical outputs in Figs. 7(a) and 7(b) show that the ellipsoidal morphology of the joint is readily captured from the flow dynamics modeled. The morphology and temperature time history of the melt pool obtained numerically is plotted in Fig. 10. From Fig. 10, it is observed that the joint diameter at the point of contact between the two beads increases rapidly as the flow of the melt pool is initially dominated by the high contact angle between the two beads. Radial growth slows once the contact angle diminishes and the second stage of radial growth occurs once the melt reaches the flow temperature observed in Fig. 4(b). The maximum melt diameter is achieved once the melt pool expands through both beads and a characteristic ellipsoidal joint is formed. Further heating of the melt results in the reduction of the joint diameter as the melt pool separates from the center of the laser focus. From the temperature history depicted in Fig. 10, it is observed that the melt temperature rises in two stages. A rapid rise in temperature first occurs as heat is concentrated and a melt pool is initiated at the center of the focus and expands to fill the entire spot size. After the initial melt formation stage, the temperature within the melt pool continues to rise at a slower rate as it expands outwards toward the bundles. From Fig. 10, the two stages in the temperature time history compares with the two stages of melt morphology change. In order to avoid the void formation behavior observed in Sec. 4.2, it is desired to terminate the heat input into the fiber bundle prior to the complete separation of the melt pool. It is observed that the separation process in this stage occurs at a much slower rate than that observed in Sec. 4.2.

The two step fiber fusion process developed from the investigation of the melt flow and separation processes presented in Secs. 4.1 and 4.2 has been shown to produce repeatable axial joints between single fiber bundles. Simulation results of the melt temperature and morphology time histories show that the added

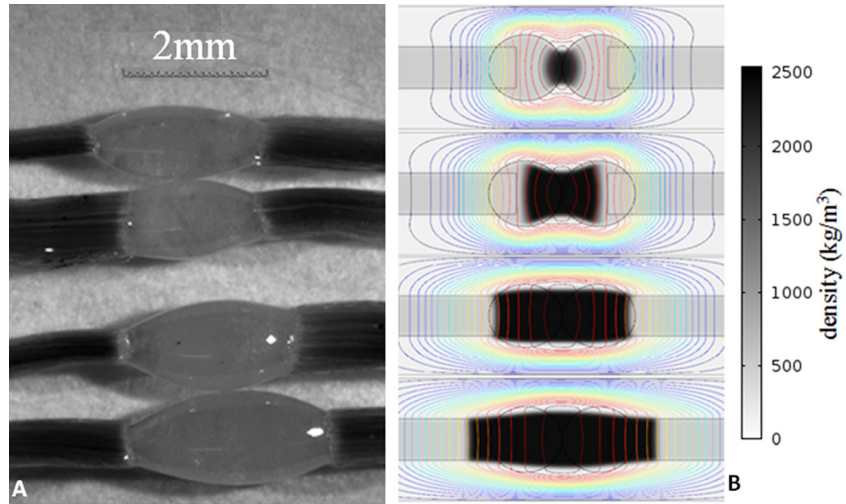


Fig. 7 (a) An optical micrograph is presented showing the joint morphologies obtained by irradiating two bundles at the point of contact between two bundles with preformed bead ends. All joint morphologies depicted are produced with similar processing times and initial bead volumes, showing good consistency and repeatability of the joining process. (b) Simulation output of the joint formation process arranged in order of increasing time: 0.1, 0.4, 1.0, and 2.0 s from top to bottom.

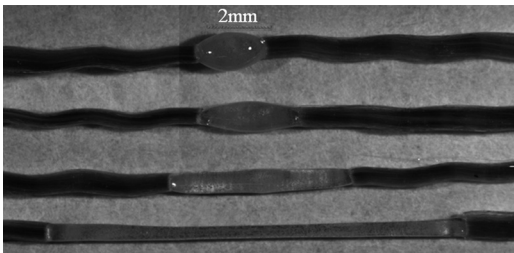


Fig. 8 An optical micrograph of joint morphologies obtained from stretching the joint to various lengths during cooling. If given the same starting melt volume, the joint diameter decreases relative to the final joint length. The morphology of the melt volume progresses from an ellipsoidal profile to a conically tapered profile when stretched. The fibers at the joint interface were also observed to compact in the radial direction when stretched.

melt volume provided by the beads serves to extend the total time required to separate the melt pool, thereby allowing for a processing window in which joining is possible. Fiber fusion joining of 3D preforms is expected to require additional glass volume in order to compensate for void formation. Although through thickness joints involve the fusion of adjacent bundles perpendicular to the fiber axis, the flow and compaction of the joints in a 3D preform is expected to follow the same characteristic behavior as that observed in single bundle experiments. Further investigation of the mechanical properties of axial fiber joints will be developed in Sec. 4.4.

4.4 Bundle Joint Strength. Tensile testing has been performed on a wide range of axially joined single bundle samples produced in the manner discussed in Sec. 4.3. Joined fiber bundles were observed to fracture near the joint rather than through the joint itself. During testing, fibers at the periphery of the joint

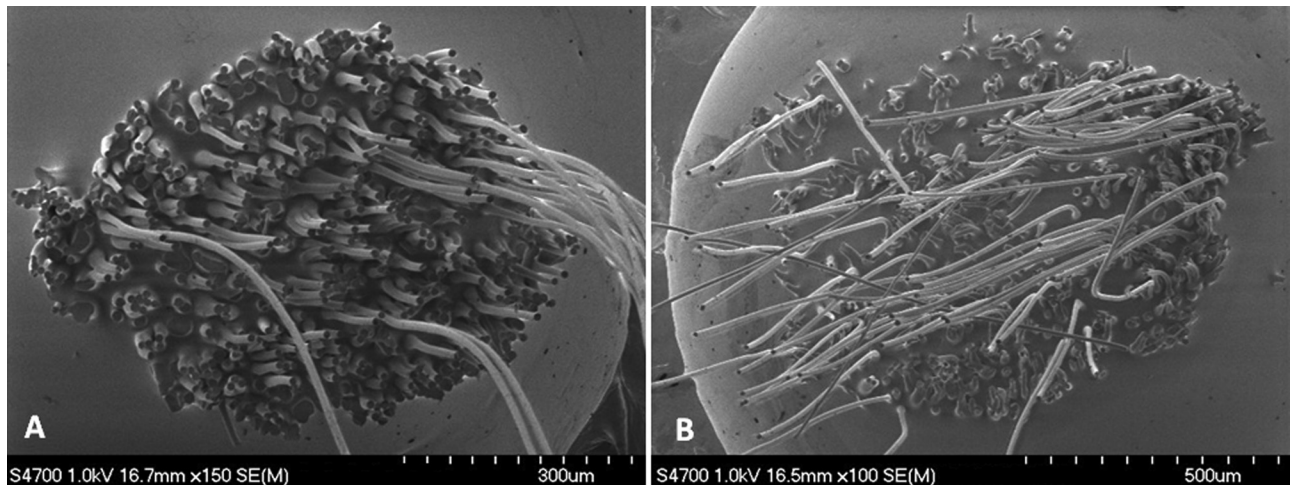


Fig. 9 (a) An SEM image of a joint interface after stretching and fracture showing high fiber packing density. (b) An SEM image of a fractured non stretched joint interface showing low fiber packing density. Fiber density is observed to be controlled by bundle confinement and stretching during the joining process. Low fiber packing density is found to be a source of added stress concentrations resulting in lower loading limits during tensile tests.

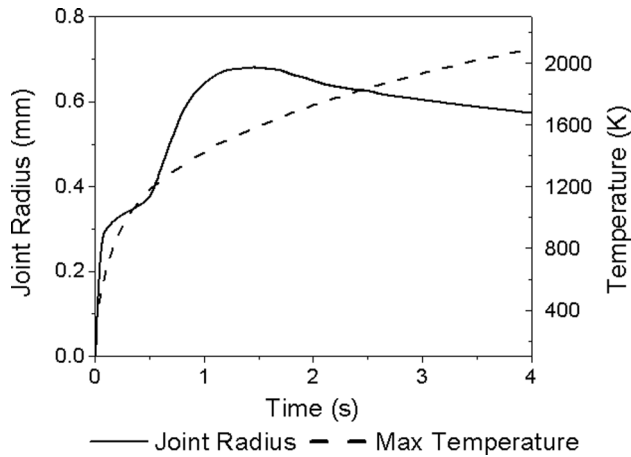


Fig. 10 The morphology and temperature simulation results of the joint formation process are plotted as a function of the simulation time. The joint radius, measured from the center of the computation domain is plotted in a solid line and the temperature history of the melt is plotted in a dotted line. The joint formation process is observed to occur in two well defined phases. The temperature of the melt is observed to increase monotonically even after the joint radius reaches a maximum.

interface consistently fractured first at the lowest loads. Post mortem SEM imaging of the fiber fracture surfaces at different regions on the joint interface depicted in Figs. 14(a) and 14(b) show significantly different failure characteristics. From these observations, it is expected that the joining process introduces a stress concentration in the fibers closest to the edge of the joints. Given the spherical or ellipsoidal morphology of the joints tested, the contact angle between the fiber and the joint is considered as the cause of the stress concentration.

In order to investigate the stress state within the joint and in the fibers along the joint interface, linear mechanical finite element modeling of the joint morphology has been carried out in the manner described in Sec. 3.2. Finite element results of spherical joint morphologies in tension show a significant stress concentration at the periphery of the joint, as depicted in Fig. 11. Finite element results show that while there is a single tensile stress component acting along the central axis at the core of the fiber bundle ($\theta = 0$), a complex stress state exists at the edge of the fiber-joint interface ($\theta = \theta_{max}$) with a significant shear component $S_{R\theta}$ acting along the tangent of the joint interface. The maximum principle stress at ($\theta = \theta_{max}$) is found to be two times the uniaxial tensile stress of a non joined fiber bundle and increase with respect to θ_{max} , as depicted in Fig. 12.

A maximum tensile strength of 50% of the stock fiber material was achieved during tensile testing, as depicted in Fig. 13(a). Critical loads below 50% were also observed in tensile test results. Effects of bundle misalignment, fiber-joint interface defects, fiber packing, and fiber density were not accounted for in the mechanical finite element modeling. The variation in fiber packing density, as depicted in post mortem SEM images in Figs. 9(a) and 9(b), is investigated as the contributing factor to the reduced strengths observed from experiments. A monotonically decreasing trend is observed between the critical tensile load and the fiber bundle diameter observed from optical micrographs, as shown in Fig. 13(b). It is believed that low fiber packing densities, corresponding to higher bundle diameters and higher fiber contact angles at the joint interface, causes higher than predicted shear stresses at the fiber-joint interface and the lower critical loads observed experimentally. Effects of other processing defects are evident from the uncertainty in the critical load depicted in Fig. 13(b).

Examination of the fiber fracture surfaces under SEM shows distinctly different fracture mechanisms between the fibers near

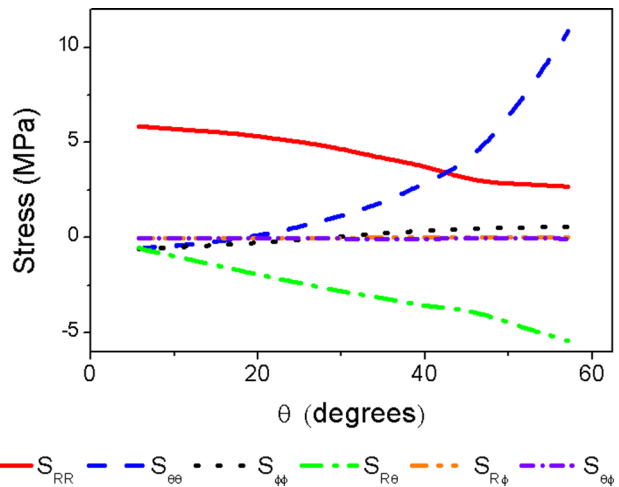


Fig. 11 The stress state along the constant radius of a spherical joint 1.2 times the diameter of a cylindrical bundle is plotted in spherical coordinates along $\phi = 0$ as a function of the contact angle θ depicted in Fig. 1. For a spherical joint diameter 1.2 times the bundle diameter, the maximum contact angle between the joint and bundle is defined at $\theta = \theta_{max} = 56.4$ deg. Shear stress components ($S_{\theta\theta}$ and $S_{R\theta}$) at edge of the joint-bundle interface ($\theta = \theta_{max}$) are observed to exceed the maximum axial stress S_{RR} at $\theta = 0$ deg.

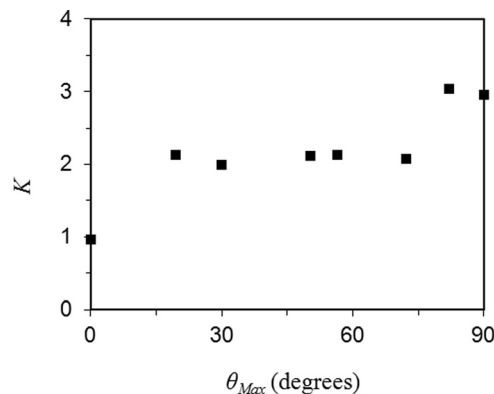


Fig. 12 Finite element results of the idealized joint morphology, depicted in Fig. 1, are plotted as a function of the maximum contact angle θ_{max} defined by the diameter of the melt bead. The stress concentration factor K , defined in Eq. (10), is the ratio of the maximum principal stress at θ_{max} to the axial stress at $\theta_{max} = 0$.

the center of the joint and those at the periphery of the joint. As observed in Fig. 14(a) the fibers in the center of the joint exhibit a flat crack surface normal to the axis of the fiber, indicative of brittle fracture under uniaxial tensile loading. Fibers on the edge of the joint, depicted in Fig. 14(b), exhibit a concave crack angled away from the fiber axis. These findings agree with the shear stress concentration found along the perimeter of the fiber bundle on the fiber-joint interface captured in the finite element solution.

Sources of stress concentrations in the joint morphology have been identified from numerical methods and confirmed through experimental findings. Fracture behavior of the joint is controlled by the shear stress located at the edge of the fiber-joint interface due to the effects of fiber contact angle and fiber packing density at the joint interface. As has been observed in this study, joint morphology and fiber packing density obtained from laser processing determines the strength and failure characteristics of the composite reinforcement. It is expected that the fiber contact angle and packing density at joint interfaces will be a main factor in

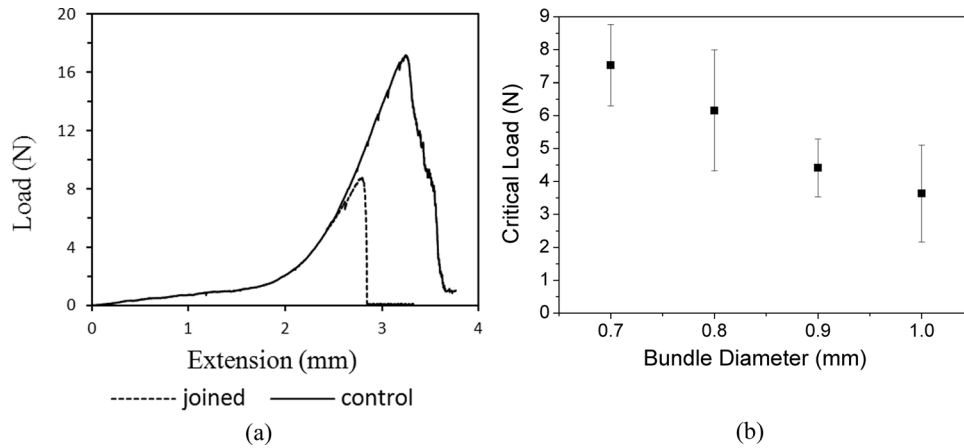


Fig. 13 (a) Typical load displacement output from single bundle tensile tests are plotted comparing the critical load achieved from a stock fiber bundle and a joined fiber bundle. Progressive failure is observed in stock fiber bundles after the critical load is reached, characterized by the sequential fracture of individual fibers. A more rapid fracture process is observed in joined samples. (b) Compiled tensile test results are plotted comparing the critical load achieved versus measured bundle diameter. Average critical load values are denoted by markers with error bars depicting the first standard deviation.

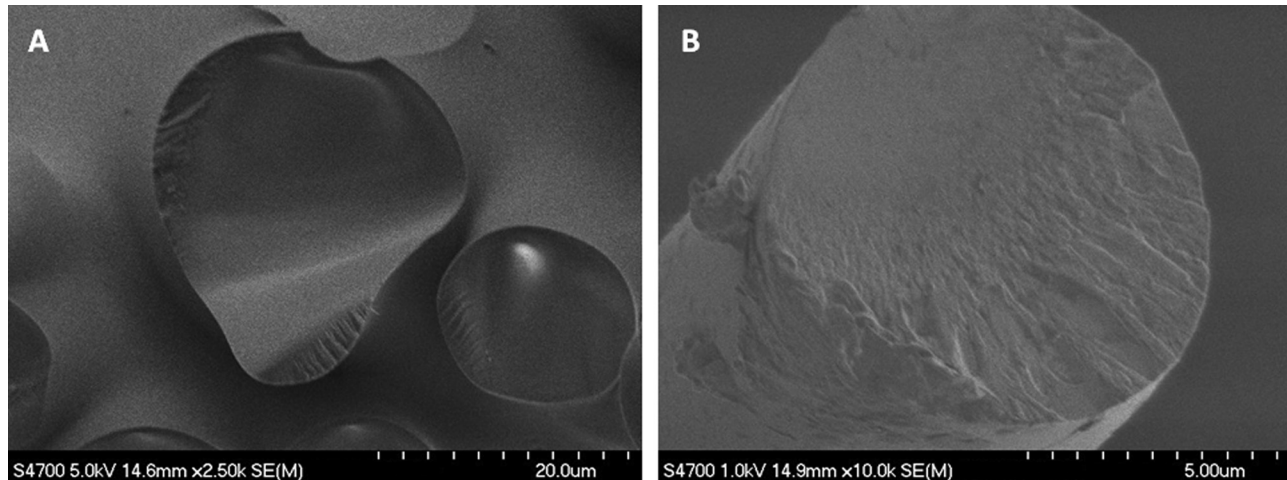


Fig. 14 (a) An SEM image of the fiber fracture surface at periphery of a joint (near $\theta = \theta_{\max}$). A concave, angled fracture surface observed in the fracture surface is indicative of a shear dominant failure mechanism in this region of the joint. Note that fibers fracture near the surface of the joint in this region and the fracture surfaces are aligned in a common direction toward the center of the joint. (b) An SEM image of a fiber fracture surface found near the center of a joint. The flat fracture surface observed in this figure is indicative of a brittle fracture due to axial tension. Fibers at the center of the joint tended to exhibit the same fracture behavior and to fracture some distance away from the joint interface.

determining the strength and fracture characteristics of a laser processed composite.

5 Conclusions

Laser fusion joining of glass fiber reinforcements has been achieved through a two step process, overcoming the compaction flow and separation effects of glass fiber bundles. Capillarity induced flow was found to be governed by the initial pore geometry and relative density of the fiber compact. Experimental investigations of the melt initiation and separation behaviors inherent in the fiber fusion process have enabled the characterization of the melt morphology under defined heating conditions. These experiments have helped to develop the understanding of the physics controlling the morphology of the melt pool.

The fiber fusion process has been studied numerically by accounting for the temperature-dependent density, conductivity and viscosity of the fiber material and shown to have good agree-

ment with experimental results of both bead formation and melt separation processes. These findings, along with the numerical models implemented, have provided the processing knowledge necessary to produce fiber to fiber joints between adjacent fiber bundles and lamina, leading to 3D fiber preform joining. Further development of these models will help to better understand the physical limitations of the fiber joining process and guide future efforts in the joining of 3D fiber preform architectures.

Mechanical testing and finite element analysis of fusion joined fiber bundles have been used to capture the internal stress state within the joint structure, highlighting the effects of morphology on the stress concentration factor and effective strength of the joint. It is shown from tensile testing and post mortem fracture surface imaging that the joint strength is highly dependent on the fiber-joint interface morphology and fiber packing density. Contact angle and fiber packing density induced stress concentrations are expected to play a major role in determining the strength and failure characteristics of laser joined 3D fiber preforms.

A fundamental investigation of the fiber fusion mechanism has been performed to evaluate the capability of laser fusion processing for the fabrication of 3D fiber preforms. Fusion joined fibers exhibit tensile strengths of the same order as stock fibers, leading to potential strength gains in the replacement of mechanical fasteners in the assembly of 3D composite preforms. Through thickness joint formation will involve additional material and manufacturing challenges, but will be based on the same processing principles and practices introduced in the axial joining of fibers.

Acknowledgment

The use of material testing equipment and fiber tensioning apparatus was provided by the Small Scale Mechanics Lab thanks to Professor Jeffrey Kysar. Thanks to Mr. Gen Satoh for the many discussions concerning sample preparation and testing. Partial financial support from Columbia University is gratefully acknowledged.

Nomenclature

C_p = specific heat
 \mathbf{F} = density gradient body force
 K = stress concentration factor
 T = temperature
 V_F = volume fraction
 E = Young's modulus
 G_{ij} = shear modulus
 S = stress
 d_x, d_y = laser spot size parameter
 k = thermal conductivity
 n = index of refraction
 \mathbf{u} = velocity

Greek Symbols

α = absorption coefficient
 β = body force coefficient
 χ = interface mobility factor
 ϵ = interface thickness
 η = dynamic viscosity
 ν = Poisson's ratio
 ϕ = phase variable
 ρ = density
 σ = surface tension coefficient
 θ = contact angle

References

- [1] Schwartz, M., 1992, *Composite Materials Handbook*, McGraw-Hill, New York.
- [2] Byrd, L., and Birman, V., 2006, "Effectiveness of z-Pins in Preventing Delamination of Co-Cured Composite Joints on the Example of a Double Cantilever Test," *Composites*, Part B, **37**(4–5), pp. 365–378.
- [3] Huang, H., and Waas, A. M., 2009, "Compressive Response of Z-Pinned Woven Glass Fiber Textile composite Laminates: Experiments," *Compos. Sci. Technol.*, **69**(14), pp. 2331–2337.
- [4] Mohamed, M. H., and Wetzel, K. K., 2006, "3D Woven Carbon/Glass Hybrid Spar Cap for Wind Turbine Rotor Blade," *ASME J. Sol. Energy Eng.*, **128**(4), pp. 562–573.
- [5] Cox, B. N., and Dadkhah, M. S., 1995, "The Macroscopic Elasticity of 3D Woven Composites," *J. Compos. Mater.*, **29**(6), pp. 785–819.
- [6] Bilisik, K., 2009, "Multiaxis 3D Woven Preform and Properties of Multiaxis 3D Woven and 3D Orthogonal Woven Carbon/Epoxy Composites," *J. Reinf. Plast. Compos.*, **29**(8), pp. 1173–1186.
- [7] Bogdanovich, A. E., 2006, "Advancements in Manufacturing and Applications of 3D Woven Preforms and Composites," 16th International Conference on Composite Materials, pp. 1–10.
- [8] Brandt, J., 1996, "Mechanical Performance of Composites Based on Various Three-Dimensional Woven-Fibre Preforms," *Compos. Sci. Technol.*, **56**(3), pp. 381–386.
- [9] Jones, I., 2005, "Improving Productivity and Quality With Laser Seaming of Fabrics," *Technical Textiles International*, May, pp. 35–38.
- [10] Niebel, V., Weinert, N., Gries, T., and Seliger, G., 2010, "Technology for Overlap-Free Joining of Semi-Finished Textile Products," *Recent Advances in Textile Composites*, Proceedings of the 10th International Conference on Textile Composites (TEXCOMP 10), DEStech Publications Inc., Lancaster, PA, pp. 340–345.
- [11] Scherer, G. W., 1979, "Sintering of Inhomogenous Glasses: Application to Optical Waveguides," *J. Non-Cryst. Solids*, **34**, pp. 239–256.
- [12] Rahaman, M. N., de Jonghe, L. C., Scherer, G. W., and Brook, R. J., 1987, "Creep and Densification During Sintering of Glass Powder Compacts," *J. Am. Ceram. Soc.*, **70**(10), pp. 766–774.
- [13] Kuczynski, G. C., 1949, "Study of the Sintering of Glass," *J. Appl. Phys.*, **20**(12), pp. 1160–1163.
- [14] Chen, J. C., and Churchill, S. W., 1963, "Radiant Heat Transfer in Packed Beds," *AIChE J.*, **9**(1), pp. 35–41.
- [15] Sun, W., Loeb, N. G., and Fu, Q., 2002, "Finite-Difference Time-Domain Solution of Light Scattering and Absorption by Particles in an Absorbing Medium," *Appl. Opt.*, **41**(27), pp. 5728–5743.
- [16] Wedding, B., 1974, "Measurements of High-Temperature Absorption Coefficients of Glasses," *J. Am. Ceram. Soc.*, **58**(3–4), pp. 102–105.
- [17] Kask, N. E., Radchenko, V. V., Fedorov, G. M., and Chopomyak, D. B., 1979, "Temperature Dependence of the Absorption Coefficient of Optical Glasses Exposed to Laser Radiation," *Sov. J. Quantum Electron.*, **9**(2), pp. 193–198.
- [18] Gardon, R., 1954, "Review of Radiant Heat Transfer in Glass," *J. Am. Ceram. Soc.*, **44**(7), pp. 305–312.
- [19] Dvurechensky, A. V., Petrov, V. A., and Reznik, V. Y., 1979, "Spectral Emissivity and Absorption Coefficient of Silica Glass at Extremely High Temperatures in the Semitransparent Region," *Infrared Phys.*, **19**, pp. 465–469.
- [20] Kingery, W. D., and Berg, M., 1955, "Study of the Initial Stages of Sintering Solids by Viscous Flow, Evaporation-Condensation, and Self-Diffusion," *J. Appl. Phys.*, **26**(10), pp. 1205–1212.
- [21] Barrett, J. W., Blowey, J. F., and Garcke, H., 1999, "Finite Element Approximation of the Cahn-Hilliard Equation With Degenerate Mobility," *SIAM J. Numer. Anal.*, **37**(1), pp. 286–318.
- [22] Dupuy, P. M., Ferdinando, M., Jakobsen, H. A., and Svendsen, H. F., 2010, "Using Cahn-Hilliard Mobility to Simulate Coalescence Dynamics," *Comput. Math. Appl.*, **59**(7), pp. 2246–2259.
- [23] Fluegel, A., 2007, "Glass Viscosity Calculation Based on a Global Statistical Modelling Approach," *Glass Technol.*, **48**(1), pp. 13–30.
- [24] Grove, F. J., 1961, "Spectral Transmission of Glass at High Temperatures and Its Application to Heat-Transfer Problems," *J. Am. Ceram. Soc.*, **44**(7), pp. 1956–1959.
- [25] Condon, E. U., 1968, "Radiative Transport in Hot Glass," *J. Quant. Spectrosc. Radiat. Transf.*, **8**, pp. 369–385.
- [26] Scherer, G. W., 1991, "Cell Models for Viscous Sintering," *J. Am. Ceram. Soc.*, **74**(7), pp. 1523–1531.